

# SCIENTIFIC REPORTS

OPEN

## Three-dimensional resistivity and switching between correlated electronic states in 1T-TaS<sub>2</sub>

Damjan Svetin<sup>1,2</sup>, Igor Vaskivskiy<sup>1,3</sup>, Serguei Brazovskii<sup>4</sup> & Dragan Mihailovic<sup>1,2,3</sup>

Received: 30 March 2016

Accepted: 28 February 2017

Published: 12 April 2017

Recent demonstrations of controlled switching between different ordered macroscopic states by impulsive electromagnetic perturbations in complex materials have opened some fundamental questions on the mechanisms responsible for such remarkable behavior. Here we experimentally address the question of whether two-dimensional (2D) Mott physics can be responsible for unusual switching between states of different electronic order in the layered dichalcogenide 1T-TaS<sub>2</sub>, or it is a result of subtle inter-layer “orbitronic” re-ordering of its stacking structure. We report on in-plane (IP) and out-of-plane (OP) resistance switching by current-pulse injection at low temperatures. Elucidating the controversial theoretical predictions, we also report on measurements of the anisotropy of the electrical resistivity  $\frac{\rho_{\perp}}{\rho_{\parallel}}$  below room temperature. From the T-dependence of  $\rho_{\perp}$  and  $\rho_{\parallel}$ , we surmise that the resistivity is more consistent with collective motion than single particle diffusive or band-like transport. The relaxation dynamics of the metastable state for both IP and OP electron transport are seemingly governed by the same mesoscopic quantum re-ordering process. We conclude that 1T-TaS<sub>2</sub> shows resistance switching arising from an interplay of both IP and OP correlations.

Layered transition metal chalcogenides are attracting general interest as very versatile and multifunctional quasi-two-dimensional materials displaying competing charge density wave order (CDW), orbital order, superconductivity, and in some cases, magnetic order. 1T-TaS<sub>2</sub> is of particular interest, as it is thought to satisfy the conditions for an unusual low-temperature Mott insulating state in which the electronic charge density within each layer is modulated by a three-directional IP CDW. This state may be described as a hexagonal array of polarons in the form of the star of David (Fig. 1a,c), defined by the Ta displacements towards the central charged Ta atom (Fig. 1a,b)<sup>1</sup>. The resulting low temperature (C) structure is commensurate with the underlying lattice (Fig. 1b,c), but spin ordering of the localized electrons at the polaron center is frustrated within the hexagonal lattice<sup>2</sup>, and no magnetic ordering has been reported so far. On heating above 220 K<sup>3</sup> the commensurate state first breaks up into a striped polaron state around 220 K, and eventually to a patchy state of nearly commensurate (NC) domains separated by domain walls above 280 K. The material becomes superconducting under pressure<sup>4</sup> or upon doping<sup>5–7</sup>. The electronic ordering perpendicular to the TaS<sub>2</sub> layers and its role in determining out-of-plane (OP) transport and phase stability is currently highly controversial. Mechanically the material behaves as a 2-dimensional Van der Waals solid, with exfoliation properties similar to graphene, which at first sight suggests the inter-layer coupling to be weak. However, band structure calculations so far<sup>8–13</sup> consistently predict insulating in-plane (IP) transport, with metallic out-of-plane (OP) transport. The latter is attributed to a highly dispersed band crossing the Fermi level along the OP,  $\Gamma$ –A direction in the Brillouin zone. The coherent OP transport in this band may be disrupted either by random interlayer stacking disorder possibly in combination with pair-wise layer stacking<sup>10</sup> or helical disorder<sup>14</sup>, leading to Anderson localization and insulating resistivity behavior at low temperatures. In addition, the Coulomb repulsion between electrons on polaron sites are expected to lead to a Mott gap in the C state. The unusual duality in the predicted electronic transport and mechanical properties could be partly reconciled if we consider that transport relies on the overlap of  $z^2$  orbitals of Ta atoms on adjacent planes, while the mechanical properties depend on weak bonding by orbitals far from the Fermi level and Coulomb interactions between Ta and S layers<sup>12</sup>. However,

<sup>1</sup>Jozef Stefan Institute, Jamova 39, 1000 Ljubljana, Slovenia. <sup>2</sup>Jozef Stefan International Postgraduate School, Jamova 39, 1000 Ljubljana, Slovenia. <sup>3</sup>CENN-Nanocenter, Jamova 39, 1000 Ljubljana, Slovenia. <sup>4</sup>Laboratory of Theoretical Physics and Statistical Models LPTMS–CNRS, UMR 8626, Université Paris-Sud Paris-Saclay, F-91405 Orsay, France. Correspondence and requests for materials should be addressed to D.M. (email: dragan.mihailovic@ijs.si)

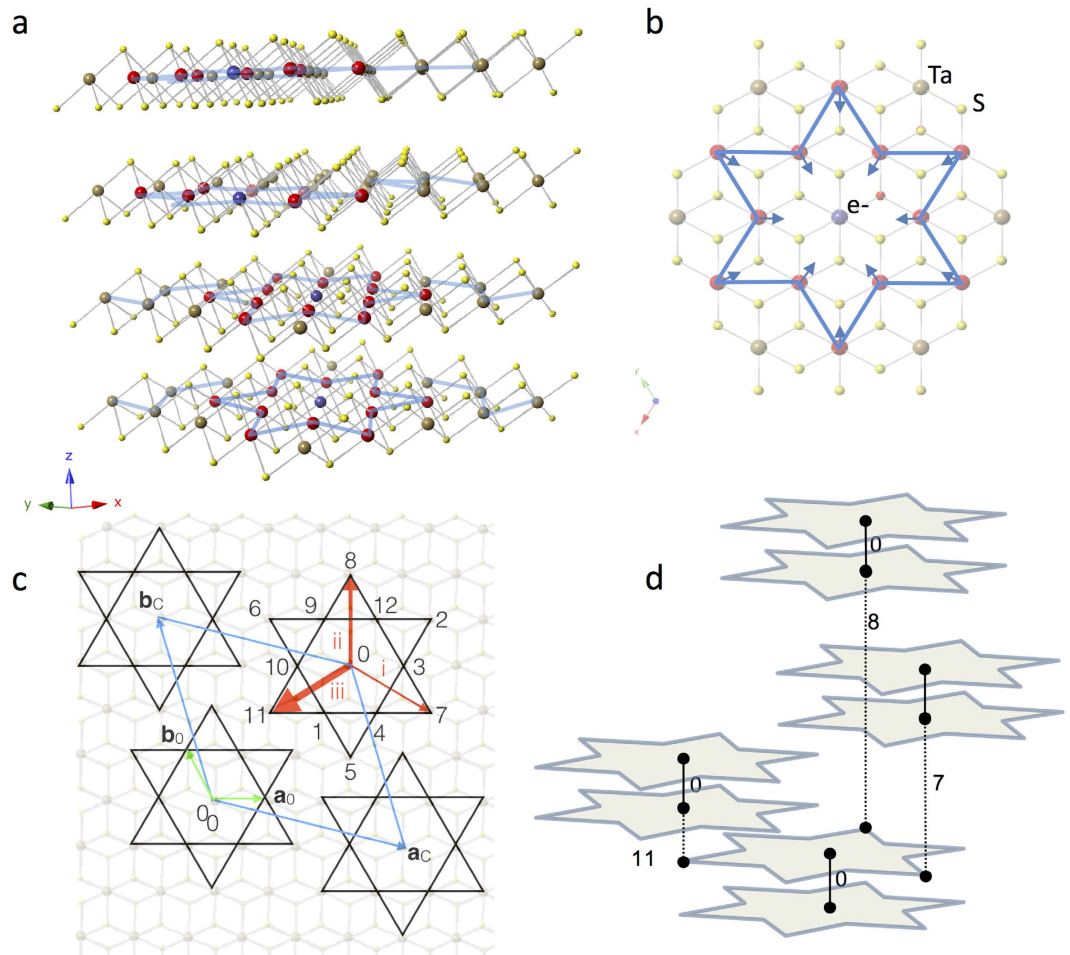


**Figure 1. The charge density wave polaronic structure and interplane stacking in the commensurate phase of 1T-TaS<sub>2</sub>.** (a) Each layer supports its own CDW, which may be viewed as a hexagonal array of polarons. The Ta atom at the centre of each polaron is colored blue, while the displaced Ta atoms are red. The extent of each polaron is schematically indicated by the blue line. (b) The detailed structure of the polaron showing atomic displacements. (c) Definition of the lattice and the CDW basis vectors within the commensurate in-plane structure and the lattice positions defining the stacking order according to ref. 14 (d) the C state helical layer stacking in the sequence 0-11-0-7-0-8-0... observed by Ishiguro and Sato<sup>14</sup>.

in the absence of systematic transport measurements and electronic structure along the *c* axis, the issue of OP interactions, and indeed the importance of the IP correlations remain unresolved.

1T-TaS<sub>2</sub> has recently attracted further attention because it was shown to exhibit sub-35 fs photo-induced<sup>15</sup> resistance switching to a hidden (H) CDW state, with similar behavior induced by 40 ps electrical pulse-injection<sup>16</sup>. Recent reports of gate-tunable state switching to a supercooled NC state at low *T*<sup>17,18</sup> and dynamical resistance switching<sup>19</sup> are also indicative of the existence of multiple competing orders at low temperature. In the H state, the relaxation properties<sup>20</sup> are strongly influenced by IP strain<sup>21</sup>, while sample thickness strongly influences the low-temperature electronic ordering<sup>17</sup> confirming a strong susceptibility of the material to external perturbations along both IP and OP directions. Currently, the mechanism for switching, and the nature of the hidden state are hotly debated, which is closely linked to the controversial nature of the low-temperature commensurate ground state itself. In particular, the question is whether the pertinent physics is confined to the individual TaS<sub>2</sub> layers, or three-dimensional stacking plays an important role in the switching and ordering<sup>8,10</sup>. Scanning tunneling microscope (STM) experiments also show switching by the tip, revealing the formation of domain walls (DWs) surrounding patches of a metallic phase in the *a*-*b* plane which is distinct from the surrounding (insulating) C state<sup>22,23</sup>. In neighboring layers, the nodes of DWs in one plane face domain centers on the neighboring planes, similar (but not the same) to that observed at higher temperatures in the NC state<sup>24</sup>. The implication is that inter-layer Coulomb interactions are not negligible.

In an attempt to resolve these questions, we address (i) the temperature dependence of OP transport, and (ii) the current-induced OP resistance switching with multi-contact measurements specifically designed for thin flakes. To elucidate the mechanism for switching, we also measure the switching dynamics and thermal relaxation

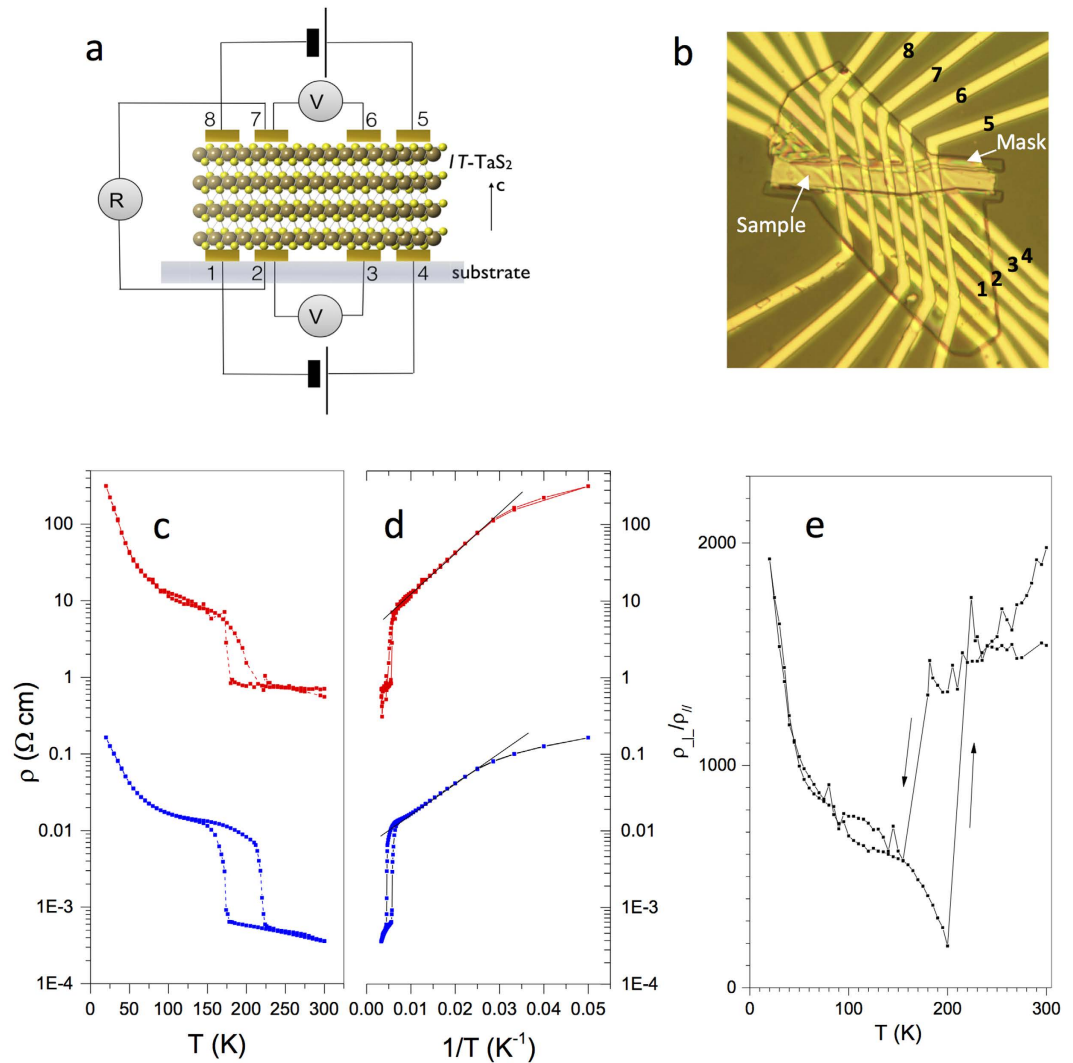


**Figure 2. The in-plane and out-of-plane resistivity of 1T-TaS<sub>2</sub> as a function of temperature measured on a multiple contact device.** (a) A schematic diagram of the circuit, (b) a microscope image of the sample showing the contact configuration. The contact spacing is 10  $\mu\text{m}$ . The masks (indicated) prevent unwanted currents through the side of the sample. (c) The in-plane resistance  $\rho_{\parallel}$  shows a 4-probe measurement (blue), while  $\rho_{\perp}$  is a 2-contact measurement, with the contact resistance subtracted (red) (see Methods). (d) An Arrhenius plot of  $\rho_{\parallel}$  (blue) and  $\rho_{\perp}$  (red) revealing activated behavior over more than one order of magnitude of resistance between 40 K and 140 K. (e) The temperature dependence of the anisotropy of the resistivity  $\rho_{\perp}/\rho_{\parallel}$  in the C state. The systematic errors are discussed in the Methods section.

properties of the metastable state in the OP direction and compare them with IP relaxation properties. The results are of fundamental importance for understanding the switching mechanism and also the OP correlations in the C ground state. On the practical side, we find that the observed c-axis switching opens the possibility of making thin film memristor devices in cross-bar geometry on polycrystalline thin films, or c-axis devices useful for ultrafast low-power low-temperature memories.

## Experimental Results

**c-axis resistance in the C state.** While the IP resistivity  $\rho_{\parallel}$  is easily measured by the conventional 4-probe method (see Methods), the c-axis resistance  $\rho_{\perp}$  of very thin flakes cannot be measured this way. However, we can obtain  $\rho_{\perp}$  by combining 2-probe and 4-probe measurements on either face of the same flake with a multiple contact device shown in Fig. 2a and b (see Methods for details). Figure 2d shows  $\rho_{\parallel}$  and  $\rho_{\perp}$  of a 75 nm thick flake of 1T-TaS<sub>2</sub>. We note a number of straightforward, yet important observations: The temperature-dependence of  $\rho_{\perp}$  is qualitatively similar to  $\rho_{\parallel}$  from 4 K to 300 K. While the magnitude of the anisotropy at intermediate temperatures  $\left(\frac{\rho_{\perp}}{\rho_{\parallel}}\right)_C \simeq 700 \sim 1000$  shown in Fig. 2e is similar to that initially reported in this temperature range<sup>25</sup>, the data show a clear dip near the NC-C transition temperature  $T_{NC-C}$ . The anisotropy then recovers to a relatively large

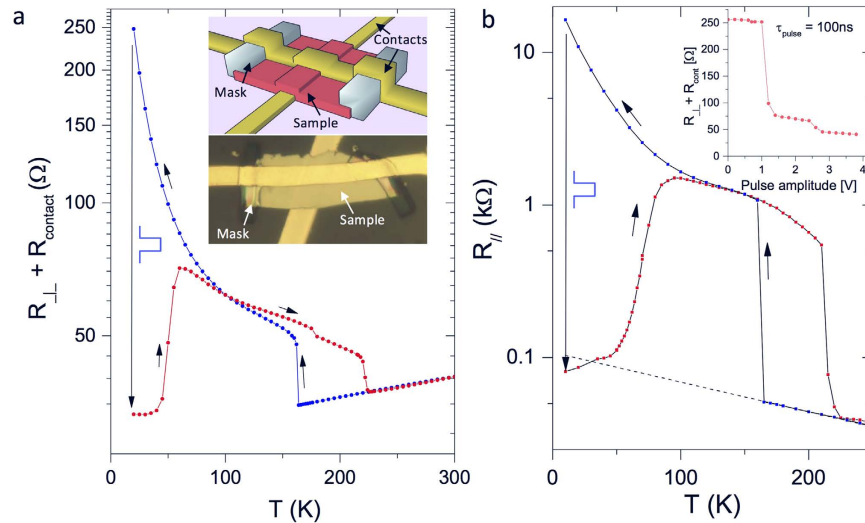


**Figure 3. Resistance switching in 1T-TaS<sub>2</sub> at 20 K.** (a) The temperature dependence of the c-axis resistance (including contacts) before (blue) and after (red) the application of a 10 V 50  $\mu$ s pulse. The insert shows the contact configuration and an image of the sample. The width of the contacts is 10  $\mu$ m. Note the mask at the edges, designed to prevent current leakage from the sides. (b) The temperature dependence of the in-plane resistance before (blue) and after (red) switching. The linearly extrapolated NC resistance is shown for reference. The insert shows the threshold for switching along the c axis with 100 ns pulses.

value of  $\sim 1500$  above  $T_{NC-C}$ . Figure 2d also shows the c-axis resistance on a logarithmic plot, revealing a dominant component that was not discussed so far<sup>26,27</sup>. Thermally activated behaviour of the form  $\rho = \rho_0 e^{-\frac{E_A}{k_B T}}$  is seen between 40 and 140 K, with similar OP and IP activation energies of  $E_A = 112 \pm 10$  K and  $91 \pm 10$  K respectively. Below 40 K, the Arrhenius plot (Fig. 2d) clearly shows that there is downturn in the resistivity with respect to the activated behavior. It's known that  $\rho_{||}$  in this temperature range is sample dependent. Uchida *et al.*<sup>28</sup> associated the presence of the upturn at low temperatures with higher quality samples and fewer impurities, which is consistent with the behavior reported upon Fe doping or substitution of S with Se<sup>5,7</sup>. The significance of the T-dependence data in the context of theory will be addressed in the Discussion.

**Resistance switching.** This is performed with 2 contacts on either side of a 90 nm thick flake, as shown in the insert to Fig. 3a. The application of a 10 V, 50  $\mu$ s pulse at 20 K causes switching to a persistent low-resistance state. For comparison, the IP resistance switching is shown in Fig. 3b. Remarkably, the measured critical threshold current densities for switching are very similar:  $i_{\perp}^T \sim 10^{-3} \frac{A}{\mu m^2}$  and  $i_{||}^T \sim 1.7 \times 10^{-3} \frac{A}{\mu m^2}$  respectively. Note that the value of the resistance  $R_H$  after switching is typically different than the extrapolated NC-state resistance, implying that the H state is distinct from the supercooled NC state reached by gating of very thin flakes in a FET configuration<sup>17</sup>. Performing the switching experiment on the device shown in Fig. 2, qualitatively the same behavior is observed for each opposite pair of contacts. Remarkably, we observe that each of the contact pairs 1–8, 2–7, 3–6 and 4–5 as shown in Fig. 2a,b, can be switched independently, implying that there is no IP cross-talk between adjacent contact pairs (or cells). The final state 2-contact resistance as a function of applied pulse amplitude is shown in the insert to Fig. 3b (Note that the contact resistance is not subtracted here). We see clear saturation behavior of  $R_H$  with two plateaus above 1 V, presumably corresponding to two different metastable states.

**Relaxation of the H state.** The relaxation behavior of the H state resistance at different temperatures is summarized in Fig. 4. Above 35 K, the relaxation process is visible on a timescale of hours. The relaxation rate increases rapidly with increasing temperature, and above 50 K it is too fast to measure with the present apparatus. During the course of the relaxation, the resistance shows discrete jumps, in agreement with previous IP relaxation<sup>20</sup>. The OP relaxation curve is fit to a simple thermally activated law:  $R = R_0 \left( 1 - C \exp\left(-\frac{E_{R\perp}}{k_B T}\right) \right)$ , with  $E_{R\perp} = 650 \pm 100$  K as shown in Fig. 4b, with the magnitude of  $E_{R\perp}$  similar to those obtained for IP relaxation on sapphire substrates<sup>20</sup>. (Here the error refers to the scatter between different samples). The difference between OP and IP relaxation is that the latter requires a stretch-exponential fit with a T-dependent exponent, while the OP relaxation does not.

**Dependence on pulse length and the role of heating.** To determine the dependence of switching threshold on pulse length and to investigate thermal effects we perform pulsed measurements as shown in Fig. 5a. The resistance is measured before switching ( $R_0$ ) and at two times after switching ( $R_1$  and  $R_2$  at delays  $\tau_1$  and  $\tau_2$  respectively). Figure 5b shows the sample resistance (including contacts) as a function of time after a “write” (W) pulse for different  $\tau_W$ . Since switching to the H state is known to occur on a much faster timescale<sup>16</sup>, all we observe



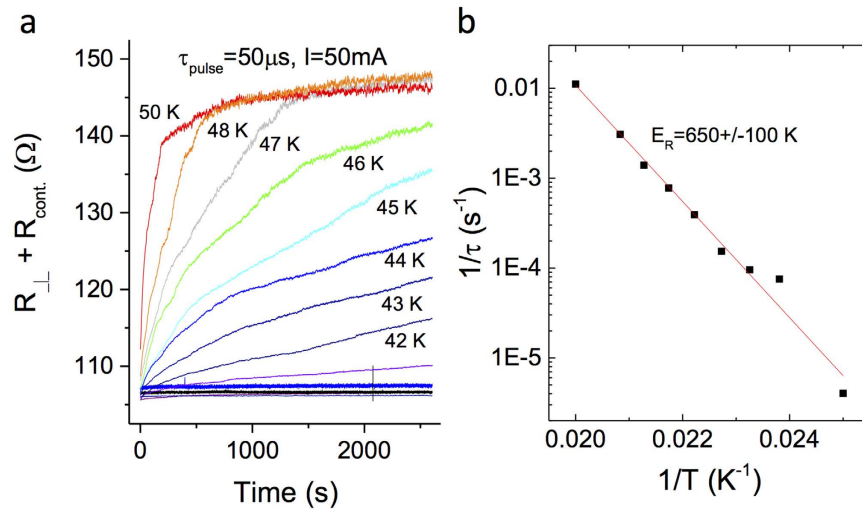


**Figure 4.** Relaxation of the H state resistance at different temperatures after switching with a  $50 \mu\text{s}$  pulse (a). Note the steps superimposed on the smooth relaxation. (b) An Arrhenius plot of the activation energy  $E_A$  obtained from the fit to the resistivity relaxation data.

here is that for short pulses with  $\tau_W < 200 \text{ ms}$ , the system remains in the H state after the W pulse. We observe from Fig. 5b that the thermal time constants are of the order of tens of seconds, and the system relaxes to equilibrium after 100 s.  $R_2$  as a function of  $\tau_W$  is shown in Fig. 5c (red squares) with  $\tau_2 = 250 \text{ s}$ . We confirm that the switching resistance values are independent of pulse length up to  $\tau_W \simeq 200 \text{ ms}$ , in agreement with previously observed IP behavior<sup>16</sup>. With  $\tau_W > 1 \text{ s}$ , the application of a pulse no longer causes any resistance change as erasure by heating becomes important.

To determine the temperature to which the pulses heat the sample, and whence the role of heating in the switching mechanism, we rely on the characteristic R-T curves in the H state and C state in Fig. 2. Since heating causes “erasure” of the H state<sup>16</sup>, the resistance measured at short times can serve as a track record of the maximum temperature reached ( $T_{\text{max}}$ ), so we can determine the thermal cycle with reasonable precision. With a delay of  $\tau_1 = 1 \text{ s}$ ,  $R_1$  corresponds approximately to the maximum temperature reached during the pulse (crosses in Fig. 5c). With  $\tau_2 = 250 \text{ s}$  the system cools to the base temperature (red squares in Fig. 5c). From Fig. 5c we see that the heating caused by short W pulses with  $\tau_W \leq 0.1 \text{ s}$  is insufficient to raise the temperature by more than a few K. Thus, for  $\tau_W < 0.1 \text{ s}$ ,  $R_1 \simeq R_2$ , as the temperature never exceeds 40 K. With  $\tau_W = 0.2 \text{ s}$ , both  $R_1$  and  $R_2$  start to increase, the H state is partly erased, and the system no longer reverts to the initial state. With  $\tau_W = 0.2 \text{ s}$ , the measured  $R_1$  corresponds to a temperature  $T = 50 \pm 5 \text{ K}$ . With increasing pulse length, the difference between  $R_1$  and  $R_2$  becomes progressively larger. For  $\tau_E \geq 2 \text{ s}$ ,  $R_1$  indicates that  $T \sim 100 \pm 5 \text{ K}$ , and  $R_1$  approaches the C state value, indicating that the H state is almost fully erased, and the system reverts to the C state. We conclude that pulses with  $\tau_E \leq 0.1 \text{ s}$  do not heat the system sufficiently to cause any thermal change of state, while thermal erasure is evident above 50 K in accordance with Fig. 2. Finally, we remark on the fact that although in principle the Joule heating can be up to 4 times larger in the C state than in the H state (because R is higher), a quadrupling of the heating with short pulses used here would still be far too small to cause thermally-induced dielectric breakdown. This confirms that the switching is electronic in origin as suggested previously for IP contacts<sup>29</sup>. Note the presence of intermediate metastable states with different resistances, depending on  $\tau_W$ , consistent with the proposed mechanism in ref. 29.

## Discussion

We first address the fundamental question of the IP and OP transport in the pristine (unswitched) state. The IP resistivity (Fig. 2c) shows a number of different regimes in different temperature ranges of the C state and is sample-dependent, so the following discussion should be understood in this context. The low-T behaviour has been attributed to either Anderson localization<sup>26</sup>, or a Mott gap splitting of the Ta  $5d_{z^2}$  band at the Fermi level<sup>30</sup>. The presence of a clear gap in the density of states at the Fermi level seen by angle resolved photoemission<sup>31–33</sup> and recent STM measurements is not consistent with either a simple Mott gap or Anderson localization. The observed behavior presented in Fig. 2 is also clearly not consistent with ordinary coherent OP band transport: the large observed anisotropy is quite in the opposite direction to what would be expected in that case. Its T-dependence (Fig. 2e) conveys some interesting information, however. Near the C-NC transition, the anisotropy strongly drops, showing a lag (hysteresis) between OP and IP behavior upon warming, implying that OP coherence is lost first, followed by the IP coherence. The more slowly varying anisotropy  $\frac{\rho_{\perp}}{\rho_{\parallel}} = 500 \sim 800$  in the intermediate temperature range between 40 and 140 K is evident in the region where well-defined thermally activated behavior is observed. The relatively large resistivity anisotropy is  $\frac{\rho_{\perp}}{\rho_{\parallel}} = 1500 \sim 1800$  in the NC state and it similar value in the

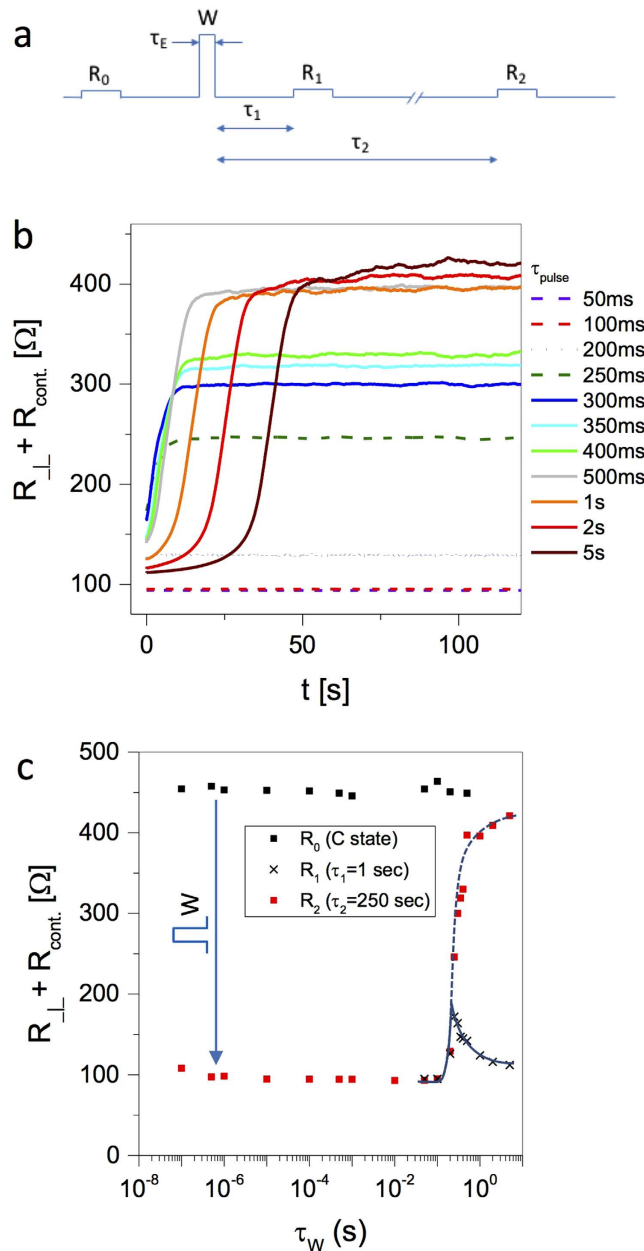


**Figure 5. Resistance switching and erasure with different  $W$  pulse lengths  $\tau_W$ .** (a) The pulse sequence used for the measurement of  $R_0$ ,  $R_1$  and  $R_2$ . (b) Evolution of the sample resistance (incl. contacts) after  $W$  pulses of different length, as indicated. The thermal time constant is seen to be  $\sim 10$  s. (c) The total OP resistance  $R_{\perp} + R_{\text{cont.}}$  before ( $R_0$ , black squares), and after the  $W$  pulse measured with  $\tau_2 = 250$  s ( $R_2$ , red squares) and  $\tau_2 = 1$  s (crosses) for different  $\tau_W$ . The latter is a measure of sample heating. The sample is reset each time by heating to 300 K in between data points. The lines are guides to the eye.

C state implies that the intrinsic anisotropy for the electron transport is not directly linked to the IP ordering in either state.

In the NC state it was shown by Bovet *et al.*<sup>12</sup> that columns of central Ta atoms with overlapping  $z^2$  orbitals give rise to half-filled 1D bands. In a strictly 1D half-filled band, the Mott insulator gap  $\Delta_{1D}$  opens with no threshold, which is not true in higher dimensions, even for an arbitrarily small Coulomb repulsion  $U_{1D}$ , irrespective of the bandwidth  $W_{1D}$ . In 1T-TaS<sub>2</sub> there is agreement that  $W_{1D} \sim 0.45$  eV<sup>8–10</sup>. On the other hand, according to recent arguments<sup>8</sup> the effective  $U_{1D} \sim 0.2$  eV should be considered, rather than the much larger single-atom value taken in to emulate the Mott gap<sup>11</sup>. The resulting gap, roughly  $\Delta_{1D} \propto W_{1D} \exp(-W_{1D}/U_{1D})$ , will compete with the small in-plane bandwidth  $W_{2D} \approx 0.1$  eV – and both can easily have comparable values. Another –diagonal– type of the inter-chain ordering was also recently considered<sup>8,10</sup>, with no inter-plane overlapping chains. In this case  $W_{1D}$  is reduced three times while  $W_{2D}$  is doubled. That would bring about a picture of a 3D narrow-band system where all bandwidths are comparable among themselves and with the Coulomb repulsion, so although the system is

prone to the conventional Mott effect in the NC state, but there is no single dominant transport mechanism. ARPES shows gapless behavior near the Fermi energy, so there is no apparent inconsistency.

The situation is different in the C state where ARPES shows a large gap<sup>9</sup>. To try and better understand the *c*-axis transport in at low temperatures, let us consider the stacking structure in more detail. Full refinement of the structure from electron diffraction measurements by Ishiguro<sup>14</sup> showed that the *c*-axis ordering in the C-state is formed by units of double 1T-TaS<sub>2</sub> layers with overlapping David stars with the double layers shifted relative to each other by  $a_0 - b_0$ ,  $a_0 + 2b_0$  or  $-2a_0 - b_0$  respectively as illustrated in Fig. 1d. Here  $a_0$  and  $b_0$  are the lattice constants of the undistorted lattice defined in Fig. 1c. With such helical stacking, the central Ta atoms are aligned within each double layer, but not between double layers, thus breaking the central Ta orbital hybridization register in the *z* direction. However, Ishiguro *et al.*<sup>14</sup> also point out that defects in the stacking order are quite common, in overall agreement with X-ray<sup>34</sup> and NMR data<sup>35</sup>, and the coherence length along the *c* axis is  $\xi_{\perp} \gtrsim 10 c_0^{10,14}$ . Phenomenological theory calculations of the stacking order by Nakanishi and Shiba<sup>36</sup> confirm that double layer stacking has a minimum energy, but also indicate that an alternative stacking configurations may exist nearby, in agreement with the observed stacking disorder in the structural data. So far, we are not aware of any microscopic calculations which include the full helical OP stacking.

Ritschel *et al.*<sup>10</sup> considered the simpler effect of two possible stackings  $T_s = 2a_c + c_c$  and  $T_s = c_c$ , where  $a_c$  and  $c_c$  are the distorted unit cell vectors in the C state, considering random bi-layer stacking along the three equivalent vectors ( $2a_c + c_c$ ,  $2b_c + c_c$  and  $-(a_c + b_c) + c_c$ ). Their band structure calculations for  $c_c$  stacking predict an IP gap and metallic behavior along the *c* axis due to a single band crossing the Fermi level along the  $\Gamma - A$  direction. For  $2a_c + c_c$  stacking, they predict metallic behavior in all three directions. Darancet *et al.*<sup>8</sup> argue that the Coulomb interaction  $U$  for IP hopping is smaller than the *c*-axis bandwidth  $W_c$ , suggesting that the Mott insulator picture of Fazekas and Tossatti<sup>2</sup> can be valid for a single layer, but not for the bulk material. In this picture<sup>8</sup>, any insulating states in bulk material that do occur in the 1T-TaS<sub>2</sub> family of materials may be regarded as arising more from OP antiferromagnetic order than from an IP Mott localization phenomenon.

Given that so far these predictions of microscopic theory are inconsistent with the data in Fig. 2, we need to discuss possible reasons. In ARPES and STM, the C and NC phases differ dramatically with the appearance of a gap in the C state, while the NC state is gapless. The sharp increase in  $\rho_{\parallel}$  at  $T_{NC-C}$  can thus be naturally attributed to the inhibition of low energy single particle excitations associated with the opening of a gap. However, in the region 40–140 K, the observed activation energy ( $E_A \approx 91$  K IP and 112 K OP) is far too small to be related to the Mott or CDW gaps whose values are at least 0.1 eV<sup>37</sup>, perhaps closer to 0.3 eV<sup>10</sup>. This energy scale  $E_A$  is not seen in any excitations which are measured by optical absorption, photoemission or tunneling. We note that these techniques detect individual single particle excitations, such as polaron binding energies or CDW gap excitations, but are not sensitive to collective polaron dynamics. The fact that the Arrhenius fit is so good over the temperature interval 40–140 K means that  $E_A$  is unlikely to be associated with random defects which would be expected to show a spread of activation energies. That also excludes the possibility that  $E_A$  corresponds to the energy difference between the Fermi level at  $E_F$  and the mobility edge  $E_M$  speaking against the Anderson localization mechanism for IP conduction in this temperature interval. Instead, the IP transport in this region is most likely related to collective polaron motion, where  $E_A$  corresponds to a well-defined transport barrier for polarons, such as may be imposed by domain walls.

Turning to the *T*-dependence of the OP transport, the remarkable similarity of the temperature-dependences of  $\rho_{\perp}(T)$  and  $\rho_{\parallel}(T)$  in all temperature regimes points towards a bottleneck mechanism which governs both IP and OP transport. OP conduction through interstitial impurities or even stacking “defects” is a very plausible mechanism for forming conducting links between layers. The OP transport thus reflects the IP mechanism, rather than being completely independent. Figure 2e shows that this is qualitatively consistent with the data over a large temperature range, except near the transition temperature  $T_{NC-C}$ . We conclude the discussion of the theory in the pristine state by noting that so far the semi-phenomenological extension of the MacMillan theory of the incommensurability<sup>36,38</sup> describes the 3D electronic ordering (including stacking) with surprising success, including the prediction of the 1<sup>st</sup> order character of the phase transitions, something which so far eludes other more recent mesoscopic models. A more economical and robust approach considers domain walls and their crossings, which enables us to understand and model the IP switching under the optical<sup>15</sup> pumping and, to an extent, the IP switching<sup>29</sup>. Further developments of microscopic theories are necessary to give a foundation for the phenomenology and derive the observable electronic properties beyond just structural information. As an outstanding problem, we note that no band structure calculations are able to reproduce the Mott insulator state. Still, the appearance of the insulating behavior in both IP and OP signifies that the emergence of the Mott state might require more sophisticated treatment than the DMFT-like calculations performed so far, at least considering the orbitronic effects of stacking. The observed behavior cannot be attributed solely to either IP ordering or OP double layer re-stacking, but indicates the existence of long-range-ordered 3D states in well-defined energy minima.

**The resistance switching mechanism.** Generically, resistance switching in dielectrics and Mott insulators is discussed as a dielectric breakdown phenomenon. The question is what is the detailed mechanism in the case of 1T-TaS<sub>2</sub>. Considering that the largest change of lattice constant upon CDW re-ordering from the NC to the C state is in the *c* direction ( $\frac{\Delta c}{c} \simeq 3 \sim 5\%$ , compared with IP change  $\frac{\Delta a}{a} \simeq 0.5 \sim 0.6\%$ )<sup>39</sup>, it is tempting to attribute the switching of the resistance to some kind of *c*-axis re-stacking. Following the calculations<sup>10</sup>, two metastable stackings of the orbitally ordered layers allow manipulation of salient features of the band structure, promoting the concept of controlling the properties of materials by using layer-stacking “orbitronics”. Indeed, competing stacking configurations were already indicated by the generalized Ginzburg-Landau-MacMillan theory<sup>36</sup>. The spin-unrestricted band calculations<sup>8</sup> attribute the sensitivity of the metal-insulator phase boundary to the nature of the inter-plane *magnetic* ordering between the localized spin  $\frac{1}{2}$  electrons at the center of each polaron. This

may lead to switching from OP antiferromagnetic - or even possibly ferromagnetic - reordering. So far the common feature of the band calculations which consider single or double layer physics is that metastability in 1T-TaS<sub>2</sub> is a consequence of »orbitronic« or stacking order, while IP order is robust and unperturbed according to these calculations

These theoretical notions are directly challenged by the observed anisotropy of the resistivity both in the pristine and the switched state (Figs 2 and 3). Moreover, recent STM studies of electrically switched 1T-TaS<sub>2</sub><sup>16,22,23</sup>, clearly show that the IP reordering is governed by the appearance of a network of domain walls (DW). The switched IP textured state is very similar to the one originally predicted<sup>15</sup> and is distinct from other states normally observed in equilibrium. Both the DWs and patches are metallic<sup>16,22,23</sup>, consistent with the conversion from polarons to itinerant states as proposed in<sup>15</sup>. The threshold current densities are quite similar for c-axis and IP switching:  $i_{\perp}^T \sim 10^{-3} \frac{A}{\mu m^2}$  and  $i_{\parallel}^T \sim 1.7 \times 10^{-3} \frac{A}{\mu m^2}$  respectively, while the applied threshold electric fields are vastly different for IP and OP switching ( $E_{\parallel}^T \sim 1 \text{ V}/\mu m$  vs.  $E_{\perp}^T \sim 100 \text{ V}/\mu m$ ). These observations are consistent with the original idea<sup>16</sup> that the switching is driven by »saturable charge injection« in such a way that once a certain number of charges are injected, the domain pattern is formed and the transformation is complete. This also explains the independence of the threshold on pulse length shown in Fig. 5c<sup>29</sup>. Also, if the layers are considered equivalent, switching is a volume effect and the threshold current densities are expected to be the same, as observed.

The relaxation data of the switched state lend further support for the notion that both IP DW formation and re-stacking occur on switching: Fig. 4 shows nearly identical behaviour and a similar activation energy as previously reported for IP resistance<sup>20</sup>. This unambiguously implies that the IP and OP relaxation is governed by the same underlying processes. While the simple exponential fit to the time-evolution of the resistivity relaxation should be considered to be an approximation for describing the Ostwald ripening nucleated growth process<sup>40,41</sup>, the fact that the IP relaxation process is better described with a stretch exponential fit<sup>20</sup>, indicates that the microscopic details of the OP relaxation are actually simpler than IP, with a single dominant energy scale given by  $E_R$ . On the other hand, the distinct steps in the relaxation process are ascribed to the relaxation of complete rows of polarons at a time as recently observed by STM<sup>16</sup>. This scenario is consistent with the topological protection mechanism which was invoked to explain the stability of the H state at low temperatures<sup>15</sup>. The two processes together explain the observed smooth relaxation superimposed on quasi-random steps shown in Fig. 4a. Direct evidence for interlayer restacking after switching comes from STM images<sup>22</sup>, which show that the switched phase is accompanied by well-defined IP phase shifts of the CDW order parameter in the topmost layer, and by a phase shift of the CDW order parameter relative to the layer underneath.

**Switching applications with an all-electronic mechanism.** Comparing the present system with other new materials showing memristive behavior currently attracting great attention, (for review see ref. 42 and the collection of articles in ref. 43 – and particularly the contribution<sup>44</sup> therein) the mechanisms are quite different. Materials of choice are oxides, chalcogenides of transition metals<sup>45–48</sup> and more complex compounds like AM<sub>4</sub>X<sub>8</sub><sup>49</sup>. They are usually considered as systems with strong electronic correlations whose fingerprint is the Mott insulator state. There are also volatile cases of the bulk metal to (Mott) insulator transition, epitomized by VO<sub>2</sub>, see ref. 42 (and 50 for elucidating the local heating mechanism), but the single crystal degradation poses a problem. In most of these cases, the switching into metastable low-resistance configurations comes from non-volatile modifications, usually in local forms of filaments or granules, associated with the manipulation of ions by the current. There are exceptions from these mechanisms of »local switching« which are more relevant to our study: the work<sup>51</sup> on Ca<sub>2</sub>RuO<sub>4</sub> and the AM<sub>4</sub>X<sub>8</sub> compounds<sup>49</sup>. There volatile, nonlocal, non-thermal switching effects have been found where the common feature seems to be electronic, rather than ionic ordering, but the phenomena are left unexplained so far. Our work, together with<sup>29</sup>, presents significant progress in comparison. Firstly, the conducting »hidden state« is truly stable within a large temperature interval. Second, the previously reported volatile switching times range from 400 ns<sup>49</sup> to tens of msec<sup>51</sup>, compared with switching between different charge-ordered electronic states in 1T-TaS<sub>2</sub> which is exceptionally fast: record electrical switching speeds below 40 ps have been reported<sup>29</sup>, limited by external electronics. Finally, all-electronic switching means that the switching energy  $E_B$  may be extremely small. Sub-atto-joule/bit values may be achievable with small devices, assuming that the theoretically predicted scaling law holds<sup>29</sup>. The fact that adjacent cells in such a device shown in Fig. 1 can be switched independently without evident cross-talk implies that useful thin-film devices with unoriented films may be constructed in either cross-bar or lateral stripline geometry, opening flexible design options for new ultrafast low-temperature memristive memory devices based on CDW state switching.

## Methods

The samples were synthesized using the vapor phase transport method<sup>26</sup>. The devices are shown in Fig. 1a,b, and Fig. 2a. Their thicknesses were measured by atomic force microscopy and are 75 and 90 nm respectively. Thin flakes of single crystal 1T-TaS<sub>2</sub> were placed over an array of contacts previously deposited on a sapphire substrate. To prevent IP current paths from the sides of the sample which might introduce an error in the measurement of the resistance perpendicular to the layers, an S8 polymer mask was then deposited at the edges of each contact as indicated. Finally, top gold contacts were made over the structure.

We cannot assume that the contact resistance is T-independent, or that the current paths are uniform between the contacts, so we need to subtract the relevant contact resistances at all temperatures without approximations. This can be done by placing 4 contacts on each side of the sample, and using a combination of 4-probe and 2-probe measurements as described in the following. Referring to Fig. 1, we name the contact resistances  $R_1, R_2, \dots, R_8$ , and the bare sample resistances between the contacts as  $R_{2-3}^s, R_{6-7}^s, R_{2-7}^s, R_{3-6}^s$ . The standard 4-probe measurement using contacts 1-2-3-4 and 5-6-7-8, sourcing the current between 1 and 2 or 5 and 8, and measuring the voltage between 2 and 3 or 6 and 7 respectively, gives us  $R_{2-3}^s$  and  $R_{6-7}^s$  respectively. The 2-probe measurements between



$R_{2-3}$  and  $R_{6-7}$  include the contact resistances such that  $R_{2-3} = R_{2-3}^s + R_2 + R_3$ ,  $R_{6-7} = R_{6-7}^s + R_6 + R_7$ ,  $R_{2-7} = R_{2-7}^s + R_2 + R_7$  and  $R_{3-6} = R_{3-6}^s + R_3 + R_6$ . From these four equations we can calculate the sum of the c-axis resistances  $R_{2-7}^s + R_{3-6}^s = R_{2-7} + R_{3-6} - [(R_{6-7} - R_{6-7}^s) - (R_{2-3} - R_{2-3}^s)]$ . Assuming uniform sample thickness  $t$  and equal contact area  $A$ , the OP resistivity is then given by  $\rho_{\perp} = (R_{2-7}^s + R_{3-6}^s)A/2t$  as plotted in Fig. 1c. The statistical error in the measurements of both IP and OP resistance is small and is indicated by the scatter of the points. Possible systematic errors for OP resistance introduced by the method are related to fact that the contact resistance on any particular contact may depend on the direction of the current, i.e. the current density distribution surrounding the actual contact for IP and OP current. This systematic error is hard to estimate, but is not likely to be more than a fraction of the contact resistance. Consequently, the qualitative picture will not be changed, and the greatest uncertainty will appear in the region where the sample resistance is smallest, i.e.  $\rho_{\perp}$  in the NC state, and the anisotropy data above 220 K (Fig. 2e), which is in any case not the main focus of this paper.

## References

1. Wilson, J. A., Disalvo, F. J. & Mahajan, S. Charge-Density Waves and Superlattices in Metallic Layered Transition-Metal Dichalcogenides. *Adv Phys* **24**, 117–201 (1975).
2. Tosatti, E. & Fazekas, P. On the nature of the low-temperature phase of 1T-TaS<sub>2</sub>. *J. Phys. Colloques* **37**, C4–165–C4–168 (1976).
3. Thomson, R., Burk, B., Zettl, A. & Clarke, J. Scanning tunneling microscopy of the charge-density-wave structure in 1T-TaS<sub>2</sub>. *Phys Rev B* **49**, 16899–16916 (1994).
4. Sips, B., Berger, H., Forro, L., Tütis, E. & Kusmartseva, A. F. From Mott state to superconductivity in 1T-TaS<sub>2</sub>. *Nature Materials* **7**, 960–965 (2008).
5. Liu, Y., Ang, R., Lu, W. J., Song, W. H. & Li, L. J. Superconductivity induced by Se-doping in layered charge-density-wave system 1T-TaS<sub>2-x</sub>Se<sub>x</sub>. *Applied Physics* **102**, 192602 (2013).
6. Ang, R. *et al.* Superconductivity and bandwidth-controlled Mott metal-insulator transition in 1 T-TaS<sub>2-x</sub>Se<sub>x</sub>. *Phys Rev B* **88**, 115145 (2013).
7. Li, L. J. *et al.* Fe-doping-induced superconductivity in the charge-density-wave system 1T-TaS<sub>2</sub>. *EPL (Europhysics Letters)* **97**, 67005 (2012).
8. Darancet, P., Millis, A. J. & Marianetti, C. A. Three-dimensional metallic and two-dimensional insulating behavior in octahedral tantalum dichalcogenides. *PRB* **90**, 045134 (2014).
9. Rossnagel, K. On the origin of charge-density waves in select layered transition-metal dichalcogenides. *J Phys-Condens Mat* **23**, 213001 (2011).
10. Ritschel, T. *et al.* Orbital textures and charge density waves in transition metal dichalcogenides. *Nat Phys* **11**, 328–331 (2015).
11. Freericks, J. K., Krishnamurthy, H. R., Ge, Y., Liu, A. Y. & Pruschke, T. Theoretical description of time-resolved pump/probe photoemission in TaS<sub>2</sub>: a single-band DFT+DMFT(NRG) study within the quasiequilibrium approximation. *Phys Status Solidi B* **246**, 948–954 (2009).
12. Bovet, M. *et al.* Interplane coupling in the quasi-two-dimensional 1T-TaS<sub>2</sub>. *Phys Rev B* **67**, 125105 (2003).
13. Rossnagel, K. & Smith, N. Spin-orbit coupling in the band structure of reconstructed 1T-TaS<sub>2</sub>. *Phys Rev B* **73**, 073106 (2006).
14. Ishiguro, T. & Sato, H. Electron microscopy of phase transformations in 1T-TaS<sub>2</sub>. *Phys Rev B* **44**, 2046–2060 (1991).
15. Stojchevska, L. *et al.* Ultrafast switching to a stable hidden quantum state in an electronic crystal. *Science adv* **344**, 177–180 (2014).
16. Vaskivskiy, I. *et al.* Fast non-thermal switching between macroscopic charge-ordered quantum states induced by charge injection. *arXiv.org cond-mat.mes-hall* (2014).
17. Yoshida, M. *et al.* Controlling charge-density-wave states in nano-thick crystals of 1T-TaS<sub>2</sub>. *Sci Rep* **4**, 7302–7307 (2014).
18. Yu, Y. *et al.* Gate-tunable phase transitions in thin flakes of 1T-TaS<sub>2</sub>. *Nat. Nanotech.* **10**, 270–276 (2015).
19. Hollander, M. J. *et al.* Electrically Driven Reversible Insulator-Metal Phase Transition in 1T-TaS<sub>2</sub>. *Nano Lett* **15**, 1861–1866 (2015).
20. Vaskivskiy, I. *et al.* Controlling the metal-to-insulator relaxation of the metastable hidden quantum state in 1T-TaS<sub>2</sub>. *Science adv* **1**, e1500168 (2015).
21. Svetin, D. *et al.* Transitions between photoinduced macroscopic quantum states in 1T-TaS<sub>2</sub> controlled by substrate strain. *Appl. Phys. Express* **7**, 103201 (2014).
22. Ma, L. *et al.* A metallic mosaic phase and the origin of Mott-insulating state in 1T-TaS<sub>2</sub>. *Nat Comm* **7**, 10956 (2016).
23. Cho, D., Cheon, S., Kim, K. S., Lee, S. H. & Cho, Y. H. Nanoscale manipulation of the Mott insulating state coupled to charge order in 1T-TaS<sub>2</sub>. *arXiv.org* (2015).
24. Spijkerman, A., de Boer, J., Meetsma, A. & Wiegers, G. X-ray crystal-structure refinement of the nearly commensurate phase of 1T-TaS<sub>2</sub> in (3 + 2)-dimensional superspace. *Phys Rev B* (1997).
25. Hambourger, P. D. & Di Salvo, F. J. Electronic conduction process in 1T-TaS<sub>2</sub>. *Physica B+C* **99**, 173–176 (1980).
26. Di Salvo, F. J. & Graebner, J. E. The low temperature electrical properties of 1T-TaS<sub>2</sub>. *Solid State Communications* **23**, 825–828 (1977).
27. Tanaka, S. & Okajima, K. Electronic Conduction in the Commensurate Charge Density Wave State of 1T-TaS<sub>2</sub>. *J. Phys. Soc. Jpn.* **53**, 2332–2341 (2013).
28. Uchida, S., Tanabe, K. & Tanaka, S. Nonlinear conduction in two-dimensional CDW system: 1T-TaS<sub>2</sub>. *Solid State Communications* **27**, 637–640 (1978).
29. Vaskivskiy, I. *et al.* Fast electronic resistance switching involving hidden charge density wave states. *Nat Comm* **7**, 11442 (2016).
30. Sato, H. *et al.* Conduction-band electronic structure of 1 T-TaS<sub>2</sub> revealed by angle-resolved inverse-photoemission spectroscopy. *Phys Rev B* **89**, 155137 (2014).
31. Cho, D. *et al.* Nanoscale manipulation of the Mott insulating state coupled to charge order in 1T-TaS<sub>2</sub>. *Nat Comm* **7**, 10453 (2016).
32. Bovet, M. *et al.* Pseudogapped Fermi surfaces of 1T-TaS<sub>2</sub> and 1T-TaSe<sub>2</sub>: A charge density wave effect. *Phys Rev B* **69** (2004).
33. Hellmann, S. *et al.* Time-domain classification of charge-density-wave insulators. *Nat Comm* **3**, 1069 (2012).
34. Tanda, S., Sambongi, T., Tani, T. & Tanaka, S. X-Ray Study of Charge Density Wave Structure in 1T-TaS<sub>2</sub>. *J. Phys. Soc. Jpn.* **53**, 476–479 (1984).
35. Naito, M., Nishihara, H. & Tanaka, S. Nuclear Magnetic Resonance and Nuclear Quadrupole Resonance Study of 181Ta in the Commensurate Charge Density Wave State of 1 T-TaS<sub>2</sub>. *J. Phys. Soc. Jpn.* **55**, 2410–2421 (1986).
36. Nakanishi, K. & Shiba, H. Theory of Three-Dimensional Orderings of Charge-Density Waves in 1T-TaX<sub>2</sub> (X: S, Se). *J. Phys. Soc. Jpn.* **53**, 1103–1113 (1984).
37. Cho, D., Cho, Y.-H., Cheong, S.-W., Kim, K.-S. & Yeom, H. W. Interplay of electron-electron and electron-phonon interactions in the low-temperature phase of TaS<sub>2</sub>. *Phys Rev B* **92**, 085132 (2015).
38. Nakanishi, K. & Shiba, H. Domain-like Incommensurate Charge-Density-Wave States and the First-Order Incommensurate-Commensurate Transitions in Layered Tantalum Dichalcogenides. I. 1T-Polytype. *J. Phys. Soc. Jpn.* **43**, 1839 (1977).
39. Sezerman, O., Simpson, A. M. & Jericho, M. H. Thermal expansion of 1T-TaS<sub>2</sub> and 2H-NbSe<sub>2</sub>. *Solid State Communications* **36**, 737–740 (1980).
40. Baldan, A. Review Progress in Ostwald ripening theories and their applications to nickel-base superalloys Part I: Ostwald ripening theories. *Journal of Materials Science* **37**, 2171–2202 (2002).

41. Shneidman, V. A. Early stages of Ostwald ripening. *Phys Rev E Stat Nonlin Soft Matter Phys* **88**, 010401 (2013).
42. Pan, F., Gao, S., Chen, C., Song, C. & Zeng, F. Recent progress in resistive random access memories: materials, switching mechanisms, and performance. *Materials Science and Engineering R* **83**, 1–59 (2014).
43. Janod, E. *et al.* Resistive Switching in Mott Insulators and Correlated Systems. *Adv. Funct. Mater.* **25**, 6287–6305 (2015).
44. Stoliar, P. *et al.* Nonthermal and purely electronic resistive switching in a Mott memory. *PRB* **90**, 045146–6 (2014).
45. Cario, L., Corraze, B., Meerschaut, A. & Chauvet, O. Dielectric breakdown and current switching effect in the incommensurate layered compound  $(\text{LaS})_{1.196}\text{VS}_2$ . *Phys Rev B* **73**, 155116 (2006).
46. Yang, J., Pickett, M., Li, X. & Ohlberg, D. Memristive switching mechanism for metal/oxide/metal nanodevices. *Nature* (2008).
47. Hasan, M., Dong, R., Lee, D. S. & Seong, D. J. A materials approach to resistive switching memory oxides. *JSTS: Journal of ...* **8**, 66 (2008).
48. Waser, R., Waser, R., Aono, M. & Aono, M. Nanoionics-based resistive switching memories. *Nature Materials* **6**, 833–840 (2007).
49. Cario, L., Vaju, C., Corraze, B., Guiot, V. & Janod, E. Electric-field-induced resistive switching in a family of mott insulators: Towards a new class of RRAM memories. *Adv Mater* **22**, 5193–5197 (2010).
50. Kim, J., Ko, C., Frenzel, A., Ramanathan, S. & Hoffman, J. E. Nanoscale imaging and control of resistance switching in  $\text{VO}_2$  at room temperature. *Appl Phys Lett* **96**, 213106 (2010).
51. Nakamura, F. *et al.* Electric-field-induced metal maintained by current of the Mott insulator  $\text{Ca}_2\text{RuO}_4$ . *Sci Rep* **3**, 2536 (2013).

## Acknowledgements

We wish to acknowledge fruitful discussions with Peter Prelovsek, Jernej Mravlje, Rok Žitko, and Han Woong Yeom. We also thank Petra Sutar for supplying the samples. DM wishes to acknowledge funding from the ERC AdG 320602 “Trajectory”.

## Author Contributions

D.S. fabricated the circuits, performed the experiments and the analysis. I.V. performed part of the experiments and contributed to the discussion. S.B. contributed to the theoretical discussion. D.M. devised the experiments, performed the analysis and wrote the paper.

## Additional Information

**Competing Interests:** The authors declare no competing financial interests.

**How to cite this article:** Svetin, D. *et al.* Three-dimensional resistivity and switching between correlated electronic states in 1T-TaS<sub>2</sub>. *Sci. Rep.* **7**, 46048; doi: 10.1038/srep46048 (2017).

**Publisher's note:** Springer Nature remains neutral with regard to jurisdictional claims in published maps and institutional affiliations.



This work is licensed under a Creative Commons Attribution 4.0 International License. The images or other third party material in this article are included in the article's Creative Commons license, unless indicated otherwise in the credit line; if the material is not included under the Creative Commons license, users will need to obtain permission from the license holder to reproduce the material. To view a copy of this license, visit <http://creativecommons.org/licenses/by/4.0/>

© The Author(s) 2017